Acta Materialia 183 (2020) 484–492

Contents lists available at ScienceDirect

Acta Materialia

journal homepage: www.elsevier.com/locate/actamat

Full length article

Characterization of polyhedral nano-oxides and helium bubbles in an annealed nanostructured ferritic alloy

Tiberiu Stan[a,*], Yuan Wu[a], Jim Ciston[b], Takuya Yamamoto[a], G. Robert Odette[a]

[a] Materials Department, University of California Santa Barbara, Engineering II, Building 1355, Santa Barbara, CA 93106, USA
[b] National Center for Electron Microscopy, Molecular Foundry, Lawrence Berkeley National Laboratory, 1 Cyclotron Road, Berkeley, CA 94720, USA

ARTICLE INFO

Article history:
Received 23 May 2019
Revised 26 August 2019
Accepted 24 October 2019
Available online 6 November 2019

Keywords:
ODS ferritic steel
Nanostructured metals
Electron backscatter diffraction (EBSD)
Transmission electron microscopy (TEM)
High-resolution electron microscopy
Nanostructured ferritic alloy

ABSTRACT

Nanostructured ferritic alloys (NFAs) contain an ultra-high density of 2–4 nm fcc pyrochlore $Y_2Ti_2O_7$ nano-oxides (NOs) embedded in a bcc Fe-14Cr ferritic matrix. Characterization of helium interactions with NOs and associated Fe-$Y_2Ti_2O_7$ interfaces is important to the development of structural materials for nuclear fusion and fission applications. A benchmark 14YWT NFA was first annealed to coarsen the NOs, then insoluble helium was implanted at 700 °C to produce a high number density of bubbles. High-resolution scanning transmission electron microscopy characterization shows two dominant Fe-$Y_2Ti_2O_7$ crystallographic orientation relationships (cube-on-edge and cube-on-cube). The smallest NOs (≈ 2 nm) are associated with the smaller bubbles (≈ 1.5 nm), while some of the largest NOs (> 6 nm) have larger, and sometimes multiple, bubbles. NO corner {111} facets are the preferred sites for He bubble nucleation. A refined sequence of events for He trapping and bubble formation is presented. These observations offer new insight on He management in NFAs, and provide a foundation for detailed modeling studies.

1. Introduction

Nanostructured ferritic alloys (NFAs) are a revolutionary class of Fe-Cr-based oxide dispersion strengthened (ODS) steels with many outstanding mechanical, thermal, and chemical properties for nuclear applications [1–10]. NFAs have high temperature strength and stability up to 900 °C [11,12] and unmatched radiation resistance, especially with respect to managing helium generated by nuclear transmutation reactions [1,13–18]. These qualities arise from a very high density of small Y-Ti-O nano-oxides (NOs) which pin dislocations and grain boundaries, and deeply trap He resulting in the formation of small, high-pressure gas bubbles at the NO-matrix interfaces [1,2]. The bubbles further add to the radiation tolerance of NFAs by acting as recombination centers for displacement damage defects. Thus, it has been argued that NFAs can turn high He levels from a liability to an asset [1,2].

NFAs are usually processed by first ball milling metal 14Cr-Fe-Ti-W and yttria (Y_2O_3) powders, thereby forcing the practically insoluble Y and O into solution [19–21]. The mechanically alloyed powders are typically then canned, degassed and consolidated by hot isostatic pressing or hot extrusion. The Y, Ti, and O precipitate as NOs during consolidation [13,21]. NOs have been characterized using transmission electron microscopy (TEM) [20–26], atom probe tomography (APT) [27–30], small angle neutron scattering (SANS) [21,31], and x-ray diffraction (XRD) [32–35]. Typical NFA NO characteristics include average diameters $\langle d \rangle \approx 1$ to 3 nm, number densities $N \approx 10^{23-24}/m^3$ and volume fractions $f \approx 0.5$ to 1% [13,21].

A recent study by Wu et al. [22] unambiguously showed that most of the NOs in several NFA conditions are fcc pyrochlore $Y_2Ti_2O_7$ (YTO). The NO-matrix crystallographic orientation relationships (ORs) are of fundamental interest because they affect critical properties such as interface energies, structures and misfit strains, as well as NO interactions with dislocations, point defects, and He. Interface characterization is also critical to calibrating first principles and atomistic interface models [36–38]. The most common bulk ORs for embedded NOs are cube-on-cube [22,23,25] and cube-on-edge [22,25,39–41]. Three-dimensional polyhedral NOs usually have topologically dictated low index {100}, {110}, and {111} YTO facets that presumably minimize the total interface energy.

Helium management is critical for fusion reactor materials that are expected to reach end of life damage levels of ~200 displacements per atom (dpa) and transmutation-product He concentrations of ~2000 atomic parts per million (appm) [2,42]. Comprehensive first principles modeling by Jiang et al. [36,37,43] indicate that He is initially trapped in the NOs themselves at a binding energy of ≈1.4 eV. Pressurized He bubbles nucleate above

* Corresponding author. Present address: Materials Science and Engineering Department, Northwestern University, 2220 Campus Drive, Cook Hall, Rm. 2036, Evanston, IL 60208, USA
E-mail address: tiberiu.stan@northwestern.edu (T. Stan).

https://doi.org/10.1016/j.actamat.2019.10.045
1359-6454/

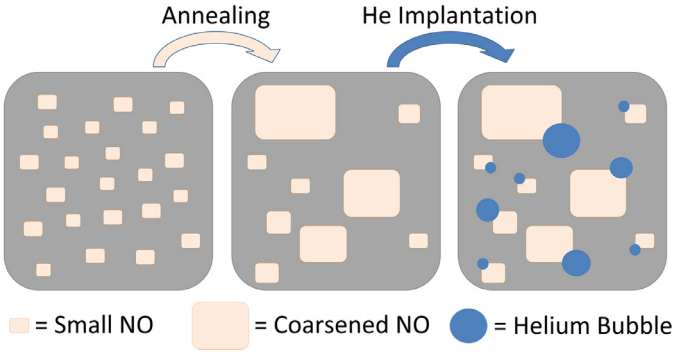

Fig. 1. A schematic of the experimental approach used in this study. A 24YWT NFA was first annealed to coarsen the NOs to ~ 6–8 nm, then He implanted at 700 °C to produce NO-associated bubbles.

a critical size when the He energy in the fluid phase is lower than in the NO. Thus, coupled with the ultra-high NO sink strength, this ensures that the fate of He is to reside in nm-scale bubbles at the oxide-matrix interfaces.

Very small NOs and bubbles (< 2 nm) are difficult to image simultaneously using conventional TEM techniques. Thus, to facilitate characterization, a 14YWT-NFA alloy was first annealed to coarsen the NOs, and subsequently He was implanted to form bubbles. A schematic of the general approach taken in this study is shown in Fig. 1. The alloy was characterized by scanning electron microscopy (SEM), electron backscatter diffraction (EBSD), bright field TEM, and high resolution scanning transmission electron microscopy (HRSTEM).

2. Materials and methods

2.1. Materials processing

General details regarding the fabrication, consolidation and initial characterization of the 14YWT class of NFAs can be found in other publications [1,21]. Milled powders were consolidated by hot isostatic pressing (HIPing) for ~1.1×10^4 s (3 h) at 1150 °C. The alloy composition is 14Cr, 0.25Y, 0.35Ti, 0.08O, 3W, 0.016Al, 0.002N, balance Fe (in units of wt%). Coupons were mechanically polished down to 0.02 µm colloidal silica, cleaned, and annealed at 1200 °C for 8.2×10^5 s (228 h) in vacuum to coarsen the NOs.

1 MeV He^+ ions were implanted at the Kyoto University DuET facility at 700 °C, at a rate of 1.2×10^{12} He/cm^2/s, for 3.6×10^4 s (10 h), producing a fluence of 4.5×10^{16} He/cm^2. The high temperature and low implantation rate were chosen so that He rapidly diffuses and is essentially all trapped at the NOs, which have a very high sink strength even in the annealed and coarsened conditions. A continuously-spinning four-window degrader foil was used to spread the implantation peak into four sample depth ranges. The resulting He concentration profile as a function of implantation depth shown in Fig. 2 was simulated using the Stopping and Range of Ions in Matter (SRIM) software. The peak He concentration is ~4100 appm at a depth of ~1 µm, and TEM examinations were carried out over the full ~1.5 µm implanted depth.

2.2. Characterization methods

Electron backscatter diffraction (EBSD) data were acquired using the CHANNEL 5 bundle on an FEI Quanta 400F scanning electron microscope (SEM). Kikuchi patterns were fit using 5 bands to ensure crystallographic accuracy. The Tango software was used to remove single isolated pixels, and images were further cleaned using low-level 8-neighbor solution fitting [44]. TEM lift-outs were fabricated using a FEI HELIOS Focused Ion Beam (FIB) tool. The foils

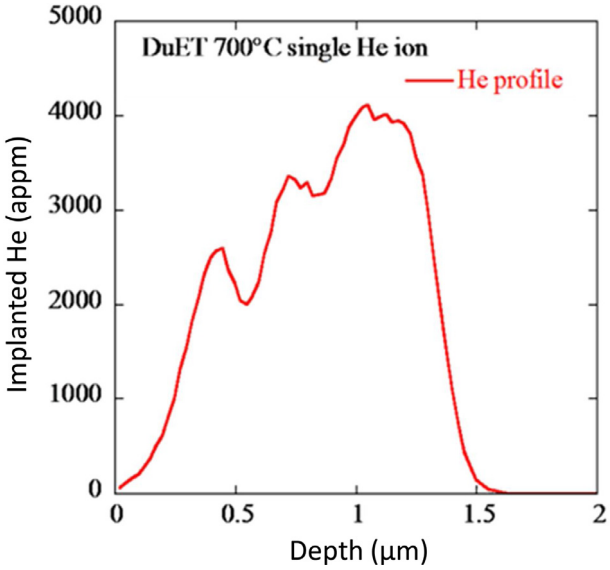

Fig. 2. A SRIM based He implantation profile. The peak He concentration is ~4100 appm at a depth of ~ 1 µm.

were cleaned using a 2 kV, 5.5 pA low energy ion beam to remove residual gallium damage. Preliminary bright field contrast TEM was carried out at the University of California Santa Barbara (UCSB) on a 300 keV FEI Titan to measure lift-out thicknesses, verify grain orientations, and to identify areas suitable for high-resolution characterization. The foils were then imaged using the 300 keV TEAM I double-aberration corrected TEM at Lawrence Berkeley National Laboratory in both high-resolution TEM (HRTEM) and HRSTEM modes. A 17 mrad convergence semiangle and 53 – 260 mrad collection angles were used to slightly emphasize diffraction contrast in order to increase visibility of the smallest oxide particles and He bubbles. General image processing, including measurements of lattice d-spacings and inter-planar angles, was carried out using ImageJ software.

3. Results

3.1. EBSD characterization

Fig. 3 shows EBSD maps of the 14YWT alloy. The band contrast image in Fig. 3a shows a wide variation in grain sizes from < 0.5 µm to > 30 µm. The inverse pole figure z-direction map in Fig. 3b is colored according to the out-of-plane crystallographic orientation of the grain (see legend in the top right of Fig. 3b). For example, a green grain indicates a {110} orientation while a red grain indicates a {100} orientation, normal to the sample surface. The annealed alloy does not exhibit preferential crystallographic texturing. EBSD was used to identify grains with <100> directions perpendicular to the surface normal.

3.2. TEM characterization

Previous SANS measurements on the as-HIPed (un-annealed) alloy indicate NOs with $\langle d \rangle \approx 3$ nm, $N \approx 7.2 \times 10^{23}/m^3$ and $f \approx 1\%$ [21]. The alloy was annealed (700 °C, 10 h) and the NO $\langle d \rangle$, N and f were measured using TEM in different grains. An inhomogeneous distribution of NOs was observed. Some grains had $\langle d \rangle \approx 7$ nm, $N \approx 1.7 \times 10^{23}/m^3$ and $f \approx 1.2\%$, while other grains had $\langle d \rangle \approx 4$ nm, $N \approx 2.6 \times 10^{23}/m^3$ and $f \approx 0.8\%$. The overall NO $\langle d \rangle$ for the annealed alloy is ≈ 6 to 8 nm, consistent with a calibrated coarsening model by Cunningham et al. [11].

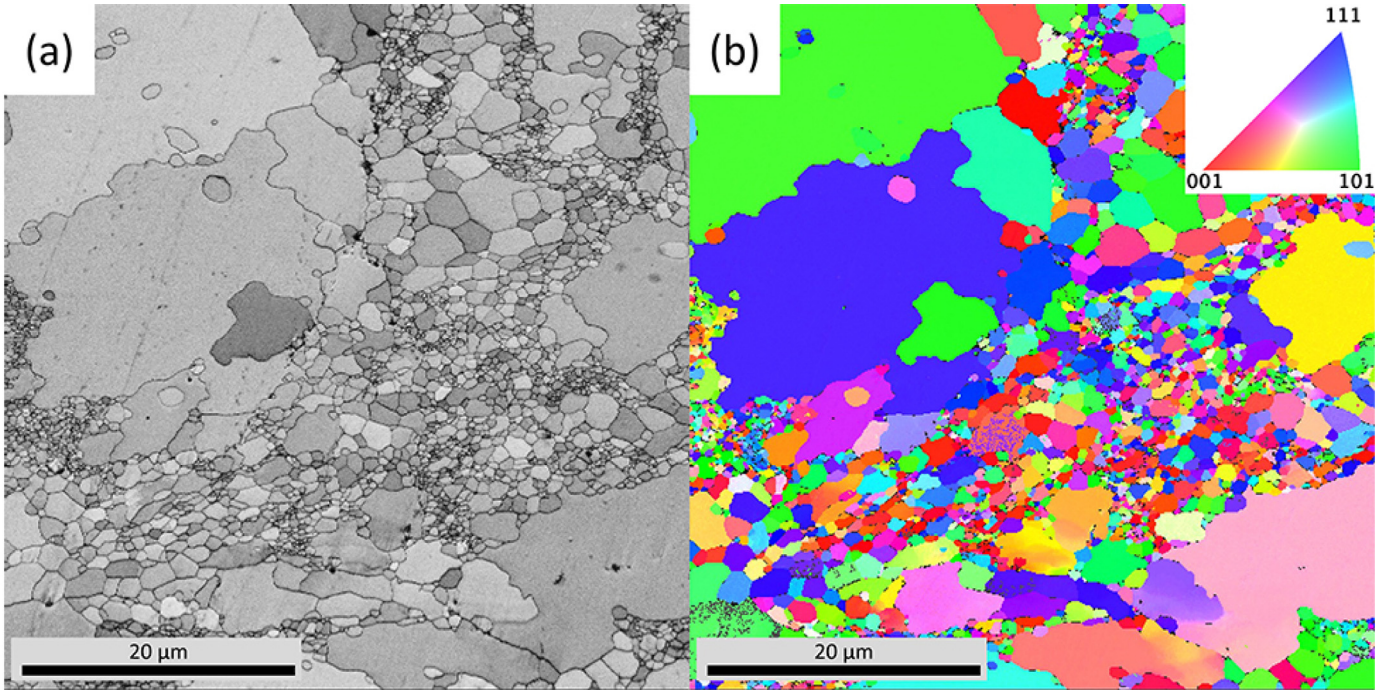

Fig. 3. (a) An EBSD band contrast map; and, (b) inverse pole figure z-direction map of the surface of the annealed 14YWT alloy.

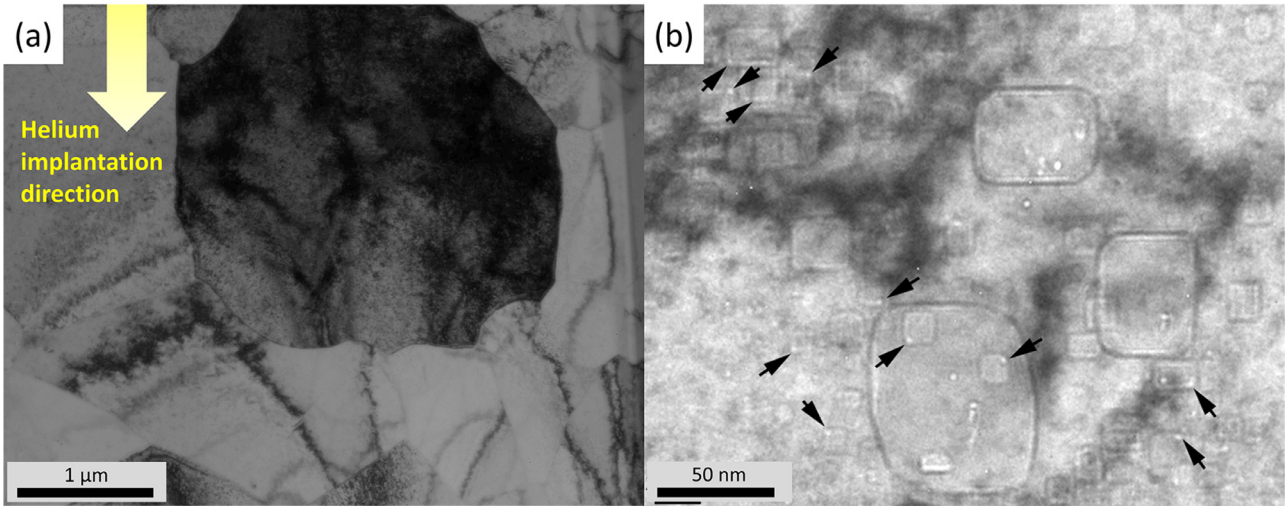

Fig. 4. (a) A low magnification bright field TEM image as viewed through the <100> zone axis; and, (b) under-focused bright field TEM image near the top region of the dark grain in (a) showing faceted NOs. The black arrows in (b) indicate He bubbles which primarily reside at NO corners.

Fig. 4a shows a low magnification cross-sectional view of the annealed 14YWT alloy. The dark $2.5 \times 2.8\,\mu m$ grain in the center of the image is viewed along the <100> zone axis. Helium was implanted through the top surface, as indicated by the yellow arrow in Fig. 4a, to a maximum depth of $\sim 1.5\,\mu m$. Fig. 4b is a higher magnification under-focused bright field TEM image from a $200 \times 180\,nm$ region just below the grain surface where the expected He concentration is < 250 appm. In the under-focused condition, the cuboidal NOs have black outlines and bubbles appear as white circles. Most bubbles in this region are found at the corners of cuboidal precipitates (black arrows in Fig. 4b). This result clearly shows that these corner facets are the preferred bubble nucleation sites on NOs.

The raw (unprocessed) HRSTEM image in Fig. 5a was collected from an implantation depth of $\sim 1\,\mu m$. In STEM imaging, the cuboidal NOs have medium intensity and the attached bubbles are darker. Fig. 5b shows the same image as Fig. 5a, but some of the NOs have been outlined in yellow, and attached bubbles in blue. As described in detail in reference [22] and also shown later in Fig. 6c, areas containing NOs have pyrochlore reflections in the Fast Fourier Transform (FFT) patterns. Two crystallographic NO-matrix bulk orientation relationships (ORs) were identified. The cube-on-cube OR {100}Fe//{100}NO and <100>Fe//<100>NO, and the cube-on-edge OR {100}Fe//{110}NO and <100>Fe//<100>NO. Two NOs with these ORs are identified in Fig. 5b. Note the larger bubbles are likely to be faceted with interfaces dictated by an inverse Wulff shape for ferrite. However, properly rendering the bubbles is complicated by their attachment to the faceted NOs and the 2D projection image of the combined 3D feature. Further, the bubbles have low contrast due to the small defocus values necessary to properly image the planes in the embedded NOs. In order to emphasize the NO facets where the bubbles form, we have chosen

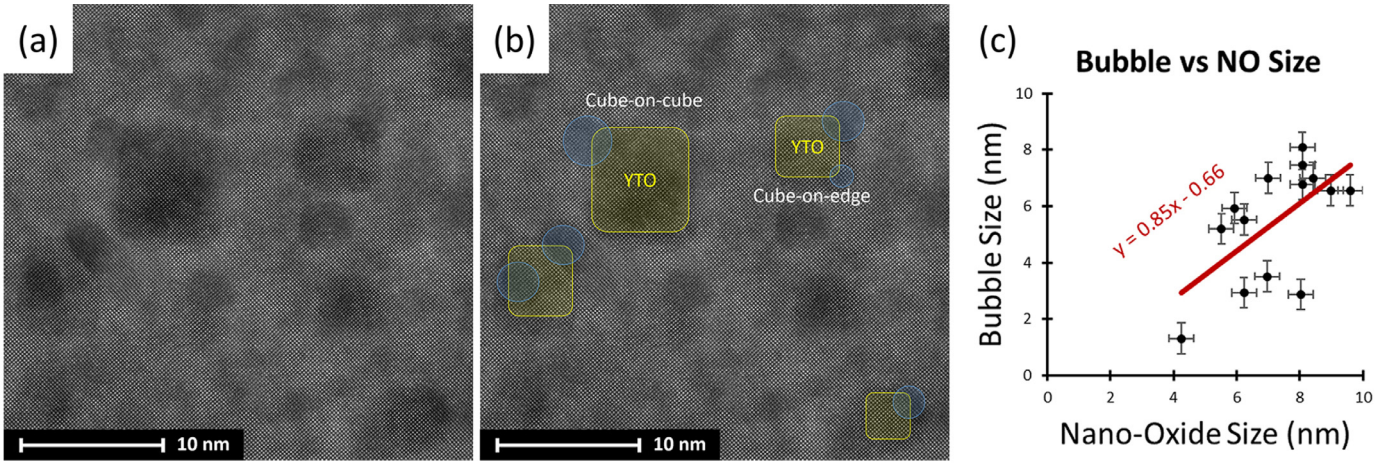

Fig. 5. (a) An unprocessed HRSTEM image of an area near the peak He implanted region showing NOs and attached bubbles; (b) the same image as (a), but with some NOs outlined in yellow and bubbles in blue; and, (c) a plot of bubble versus NO size showing a weak but positive correlation. (For interpretation of the references to colour in this figure legend, the reader is referred to the web version of this article.)

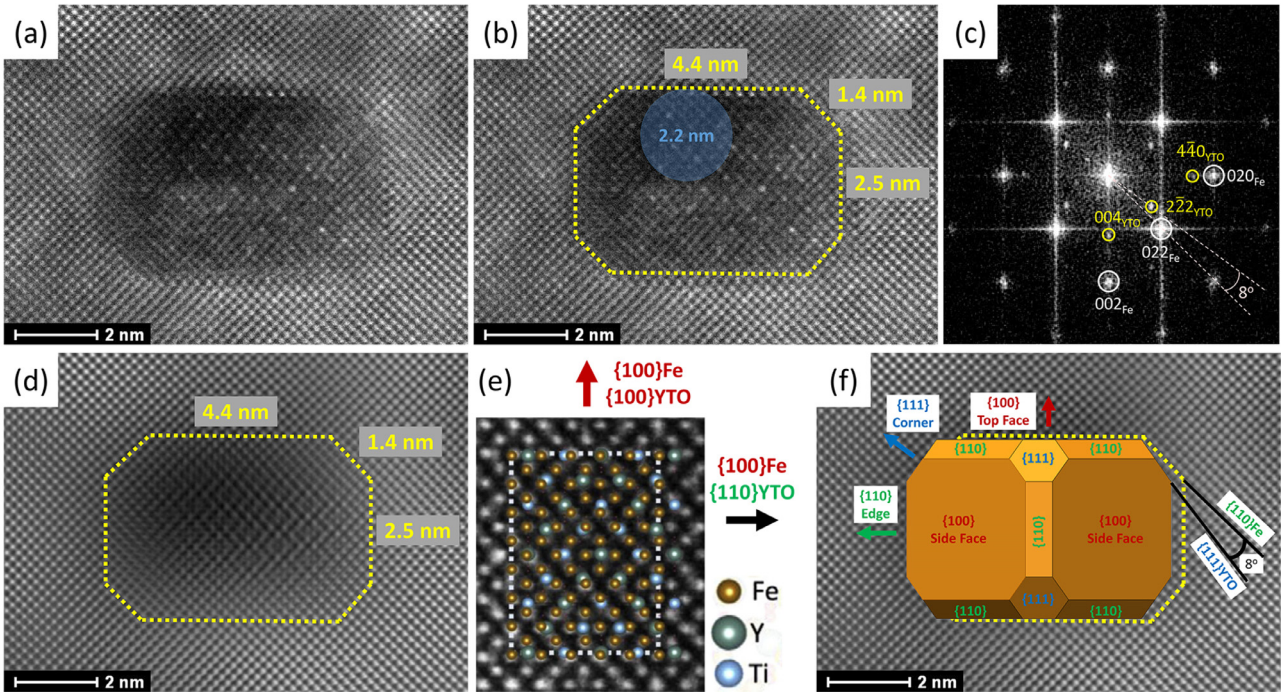

Fig. 6. (a) An unprocessed HRSTEM image as viewed along the <100> Fe zone axis; (b) an outlined image showing an embedded NO and bubble in yellow and blue, respectively; (c) the corresponding FFT pattern with YTO and Fe reflections marked with yellow and white, respectively; (d) an IFFT image showing a zig-zag pattern of atomic columns of Y, Ti, and *Y*+Ti; (e) the atomic overlay showing the cube-on-edge bulk OR; and, (f) a plausible 3D rendering of the embedded NO with labeled facets. (For interpretation of the references to colour in this figure legend, the reader is referred to the web version of this article.)

to render the bubbles as simple blue circles (Fig. 5b) or spheres (Fig. 7c). The plot in Fig. 5c shows the rough correlation between bubble size and NO size for the particles analyzed in this HRSTEM study (including those shown in Fig. 5). Only NOs with sizes ~2 to ~10 nm with clearly visible bubbles were measured. The red trend line has a positive slope of 0.85 indicating that larger NOs have larger bubbles attached to them. On average, the bubbles reach ~75% of the NO sizes. These observations are important to the general understanding and modeling of He management in NFAs.

The NO in Fig. 6 was selected for in-depth crystallographic analysis. Fig. 6a is an unprocessed HRSTEM image viewed along the <100>Fe and <110>YTO zone axis. A NO with size of ~6.5 x ~3.4 nm is outlined yellow in Fig. 6b. The dark area at the top of the NO is likely a ~2.2 nm He bubble, above or below, the NO attached to a corner facet (bubble attachment is discussed in detail in conjunction with Fig. 7). Fig. 6c shows the FFT pattern from the image in Fig. 6a. The YTO and Fe spots are labeled with yellow and white, respectively. The FFT pattern clearly shows the cube-on-edge bulk OR {100}Fe//{110}NO and <100>Fe//<100>NO, also seen in reference [22].

Fig. 6d is an Inverse Fast Fourier Transform (IFFT) image created by isolating all of the spots in the FFT in Fig. 6c for both the pyrochlore and the ferrite. This procedure filters out large wavelengths and identifies the atomic columns in the image. A zig-zag pattern is apparent in the NO, which is expected for the Fe-YTO cube-on-edge bulk OR. The pattern is clearer near the center of the NO, naturally becoming less visible near the thinner edges. Fig. 6e is a CrystalMaker rendering of the atomic positions of the cube-

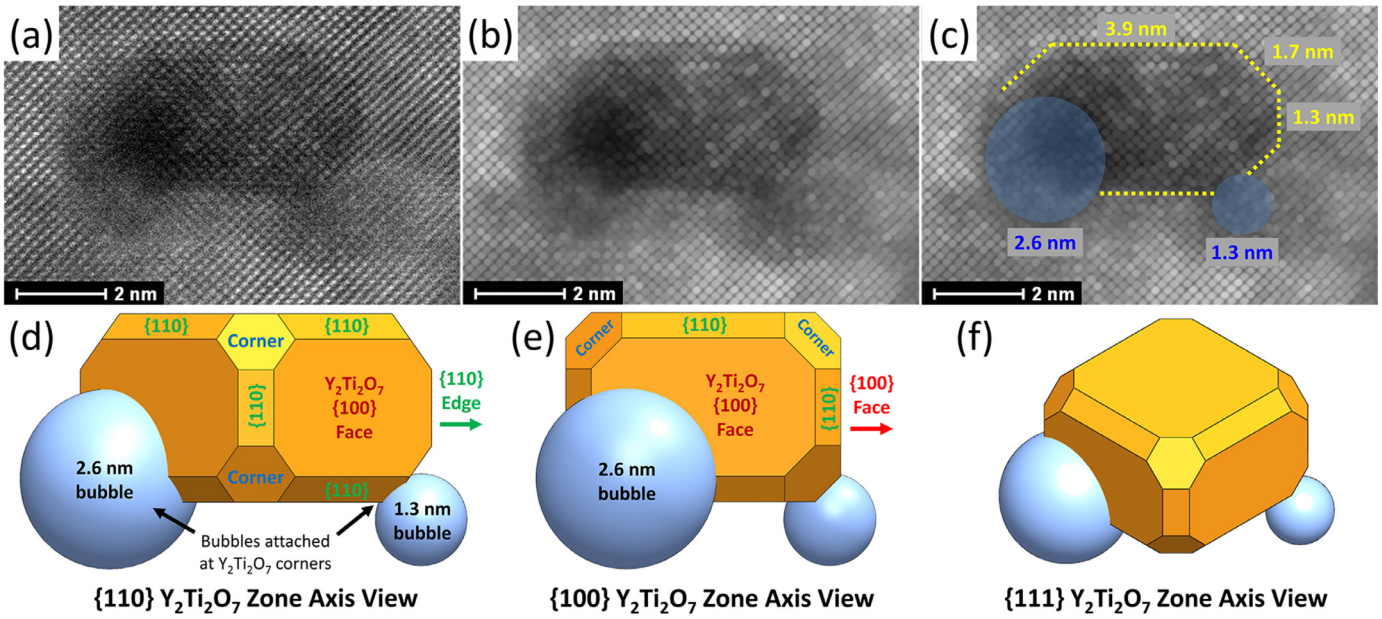

Fig. 7. (a-c) Unprocessed HRSTEM image, processed image, and processed image with outlines of a NO and two bubbles in yellow and blue, respectively; and (d-f) a 3D rendering of the NO and bubbles as viewed through the {110}, {100}, and {111} YTO directions, respectively. (For interpretation of the references to colour in this figure legend, the reader is referred to the web version of this article.)

on-edge OR, overlaid onto the zig–zag NO column pattern. Fe, Y, and Ti atoms are shown in yellow, green, and blue, respectively. These results further confirm the presence of the YTO pyrochlore structure.

A 3D reconstruction of a plausible embedded NO polyhedral shape can be obtained by combining the particle outline with the crystallographic orientation. The polyhedral shape shown in Fig. 6f is labeled with the different facet surface orientations. The top and bottom NO facets have a rotated cube-on-cube interface OR: {100}Fe//{100}NO with <100>Fe//<110>NO. Notably, this OR was observed in Fe thin film depositions on {100} $Y_2Ti_2O_7$ single crystal substrates [45]. The facets labeled "{100} Side Face" in Fig. 6f have the edge-on-cube interface OR: {110}Fe//{100}NO with <100>Fe//<100>NO. The side interfaces labeled "{110} Edge" in Fig. 6f have the cube-on-edge OR: {100}Fe//{110}NO with <100>Fe//<100>NO. Finally, the diagonal ORs labeled "{111} Corner" are close to the edge-on-corner: {110}Fe//{111}NO with <100>Fe//<110>NO. This OR is also found in thin film Fe deposition on {111} $Y_2Ti_2O_7$ single crystal substrates [46]. However, as also seen in the FFT pattern in Fig. 6c, there is an ~8° angle between the {110}Fe and {111}YTO planes. The {100}YTO facets have the largest interfaces areas, followed by the {110} and {111} facets. This is also the case for most of the NOs observed in this study. Thus, the {100} interfaces likely have the lowest interface energies (see discussion section).

Fig. 7a shows an unprocessed HRSTEM image of a NO with two He bubbles. Fig. 7b was obtained using ImageJ by smoothing Fig. 7a twice and applying a maximum grayscale dilation filter which replaces each pixel with the largest value its neighborhood. This technique was chosen over the conventional IFFT image processing because it better outlines bubble locations and sizes. Bubbles appear as darker features in STEM images that disrupt the atomic column periodicity. The two disordered areas in Fig. 7b suggest the presence of bubbles (marked with blue circles in Fig. 7c).

The faceted NO in Fig. 7c (outlined with yellow dashed lines) is roughly ~3.5 x ~5.9 nm, and has two bubbles with diameters ~2.6 nm and ~1.3 nm. A plausible 3D rendering of the NO and bubbles is shown in Fig. 7d. A FFT analysis indicates that the NO has the $Y_2Ti_2O_7$ pyrochlore structure with the same bulk OR and interfaces as the NO shown in Fig. 6. Fig. 7c and Fig. 7d show that the smaller bubble is attached to the {111} NO corner facet, while the larger bubble is centered on the {111} NO facet, but has grown to envelop the surrounding NO interfaces. Fig. 7e is the same 3D rendering as Fig. 7d, but the NO and bubbles have been rotated by 45° about the vertical axis. Fig. 7e is a visualization of the particle for the <110>Fe and <100>YTO zone axis. Fig. 7f is again the same 3D rendering, but viewed for the <111>YTO zone axis. TEM imaging only shows a 2D projection of the 3D particle, and the particle shape can be discerned by its outline. Together, Figs. 7d, e and f show how the same particle appears different depending on the imaging orientation.

4. Discussion

In this study, a 14YWT NFA was annealed to coarsen the embedded NOs, and subsequently implanted with 1 MeV He to form bubbles. EBSD results show a wide variety of grain shapes with sizes ranging from < 0.5 µm to > 30 µm. The maximum implantation depth was ≈ 1.5 µm, and similarly sized grains were selected for TEM examination. All of the inspected NOs large enough for FFT analysis (d > ~2 nm) showed the $Y_2Ti_2O_7$ pyrochlore structure. This has been established as the dominant phase for the smallest NOs in most NFAs [22,23]. The atomic-scale detail obtained using the TEAM I double-aberration corrected microscope allowed a full 3D estimation of the NO particle shapes, as illustrated in Figs. 6 and 7.

NO-matrix interface chemistries and energies (γ_{hkl}) are highly dependent on the O partial pressure (P_{O2}) [37], which are not well established. The likely thermodynamic bounds are P_{O2} levels between in equilibrium Cr_2O_3 and TiO_2, which result in non-stoichiometric Y-Ti rich interface terminations with semi-coherent energies between ≈ 0.2 - 0.8 J/m^2 [37]. However, APT studies measured higher non-equilibrium levels of unreacted excess O (due to internal oxidation kinetic limits and perhaps excess vacancies) with matrix values in the range of ≈ 0.1 at% or more [21]. In this case the interface will be highly O enriched, with semi-coherent energies < 0.8 J/m^2 [37]. First principles models indicate that Fe atoms usually match with the O atoms for both Fe-YTO [37] and

Table 1
Interface names, labels on polyhedral shown in Fig. 6, interfacial orientation relationships, facet surface areas on polyhedral, calculated interface misfit dislocation spacing, near coincidence site lattice (NCSL) area, and relative interface energies.

Interface Name	Orientation Relationship	Label on Polyhedral	Surface Area [nm^2]	Dislocation Spacing [nm]	NCSL [nm^2]	Interface Energy
rotated cube-on-cube	{100}Fe//{100}NO <100>Fe//<110>NO <110>Fe//<100>NO	{100} Top	~14.0 Largest	~1.8 x ~1.8	~3.0 Largest	Smallest
edge-on-cube	{110}Fe//{100}NO <100>Fe//<100>NO <110>Fe//<110>NO	{100} Side	~8.7 Medium	~1.8 x ~1.8	~3.0 Largest	Medium
cube-on-edge	{100}Fe//{110}NO <100>Fe//<100>NO <100>Fe//<110>NO	{110} Edge	~5.9 Medium	~1.4 x ~1.7	~2.5 Medium	Medium
edge-on-corner	{110}Fe//{111}NO <100>Fe//<110>NO <110>Fe//<112>NO	{111} Corner	~1.2 Smallest	~1.4 x ~1.2	~1.7 Smallest	Largest

Fe-Y_2O_3 [47] interfaces. Such O-rich terminations may also be partly responsible for significant segregation of Cr and Ti to the NO interfaces [21,28]. A supersphere calculation by Ribis et al. indicates primarily cube-on-cube interface energies of ≈ 0.26 J/m^2 [23], while Barnard et al. found coarsening due to pipe diffusion to be consistent with interface energies of ≈ 1.2 J/m^2 [38].

Due to the YTO pyrochlore structure and many possible interface chemistries, as well as the vastly different lattice constants between YTO (10.1 Å) and Fe (2.86 Å), it is impossible to determine how all of the matrix atoms bond with Y, Ti and O across the interfaces based purely on geometrical considerations. Even in the simplest cases, determining the complex nature of NO-matrix interfaces requires accurate first principles atomic-scale modeling such as those performed by Yang et al. [36,37,43]. The computational challenges to model all of the possible interface ORs are enormous, and in some cases practically prohibitive.

In spite of these complexities, estimates of the comparative of metal-oxide interface energies can be obtained by examining the different facet sizes and crystallographic orientations observed in the present study (Table 1). In a Wulff construction, the anisotropic interface energy γ_{hkl} is plotted in the hkl crystallographic direction at an energy scaled distance of $|\gamma_{hkl}|$ from the crystal center [48–50]. The equilibrium crystal shape is defined as the inner convex hull bounded by planes drawn perpendicular to each point along the γ_{hkl} surface. The equilibrium crystal shape minimizes $\Sigma A_{hkl}\gamma_{hkl}$ where A_{hkl} is the surface area of the plane with energy of γ_{hkl}. Figs. 6 and 7 show that the {100} facets have the largest surface areas, followed by the {110} edge facets, and then the {111} corner facets. The {100} planes are closest to the crystal geometrical center indicating a smaller γ_{100}. Therefore, the interface energies for the embedded particle are ranked as: $\gamma_{100} < \gamma_{110} < \gamma_{111}$. This ranking is consistent with NO shapes seen in other studies [22,23,25], but is not expected for free surfaces in fcc systems where {100} and {111} facets are generally dominant [48].

All four ORs observed in this study were created using CrystalMaker to further gain insight into relative interface energy magnitudes. Unstrained Fe and YTO surfaces were geometrically matched and the resulting near coincident site lattices (NCSLs) were compared. Top views are shown in Fig. 8, where the Fe-oxide interfaces are perpendicular to the viewing direction. For the interfaces with {100} YTO surfaces (Fig. 8a and b), the NCSLs exhibit two-fold symmetry, which is expected for cubic systems. However, the {110} and {111} YTO interfaces (Fig. 8c and 8c) exhibit rectangular NCSLs, thus the expected misfit dislocation spacing would vary in different directions along the biphasic boundary. Large NCSLs are indicative of large interfacial misfit dislocation spacings, large facet sizes, and small interface energies [48,51–53]. Because the atomic bonding across the Fe-YTO interface is not fully known, it is difficult to estimate the misfit dislocation network for each of the four ORs. All of the interfaces are semicoherent with misfit strains of at least ~19%, calculated using the same methods as detailed in our previous paper [39] and in reference [45]. The observed NCSL sizes are reported in Table 1. The edge-on-corner OR shown in Fig. 8d has the smallest NCSL, is the smallest observed NO facet, and thus has the largest interface energy. The 1.2 nm^2 {111} NO corner facet on the embedded NO observed in Fig. 6 is too small to fully fit the 1.8 nm^2 NCSL, further suggesting a corresponding high interface energy. The geometrical CrystalMaker study yields similar trends in interface energy ranking ($\gamma_{100} < \gamma_{110} < \gamma_{111}$) as obtained by comparing NO facet sizes.

Regarding interactions with He, nearly all of the observable NOs in the HRTEM micrographs had nm-scale bubbles attached. The larger NOs are associated with larger bubbles, and some of the largest (> 6 nm) NOs had multiple bubbles. On average, the bubble sizes reach ~75% of the NO sizes, and almost always found on {111} NO facets. The {111} YTO interface is likely a preferred nucleation site due to the high interface energy, and the ~8° mismatch between {111}YTO and {110}Fe planes, as shown in the atomic rendering in Fig. 9. The figure was created in CrystalMaker by matching perfect (un-strained) YTO and Fe lattices. Note that O atoms were omitted for clarity, and to better match the top-right corner of the embedded particle in Fig. 7c. The rendering in Fig. 9 shows a gap at the corner interface, but the actual YTO-Fe bonding in the NFA is likely complicated and presumably involves large strains or dislocations. The corner interface (roughly eight {110} Fe planes wide) with one misfit dislocation could accommodate the ~8°, but it is difficult to experimentally observe individual misfit dislocations on very small NO facets as most of the TEM signal comes from the matrix atoms above and below the embedded particle. The high-energy of this interface, along with the ~8° mismatch, rationalizes why the corner facet is the smallest and why it is a highly preferred He bubble nucleation site.

The observations in this study add to the growing general understanding regarding helium management in NFAs. An updated sequence of events is as follows. He is first produced by neutron-alpha transmutation reactions in the ferritic NFA matrix [14]. Being practically insoluble, He atoms migrate to sinks that are dominated by the YTO NOs. As shown by first-principles modeling, He enters the relatively open pyrochlore YTO structure and is deeply trapped at octahedral interstitial positions within the NOs themselves [37]. The He energy is similar at the interface, where diffusional clustering and bubble formation occurs. At very small sizes, the He energy is higher in the bubbles than in the NOs. However, classical stochastic nucleation mechanisms produce bubbles up to a critical size, at which point the He energy decreases to a value below that in the NOs, resulting in He draining into the interfacial bubbles. The bubbles preferentially nucleate at higher interface energy YTO corner facets. Conceptually, the NOs act as a “helium storage

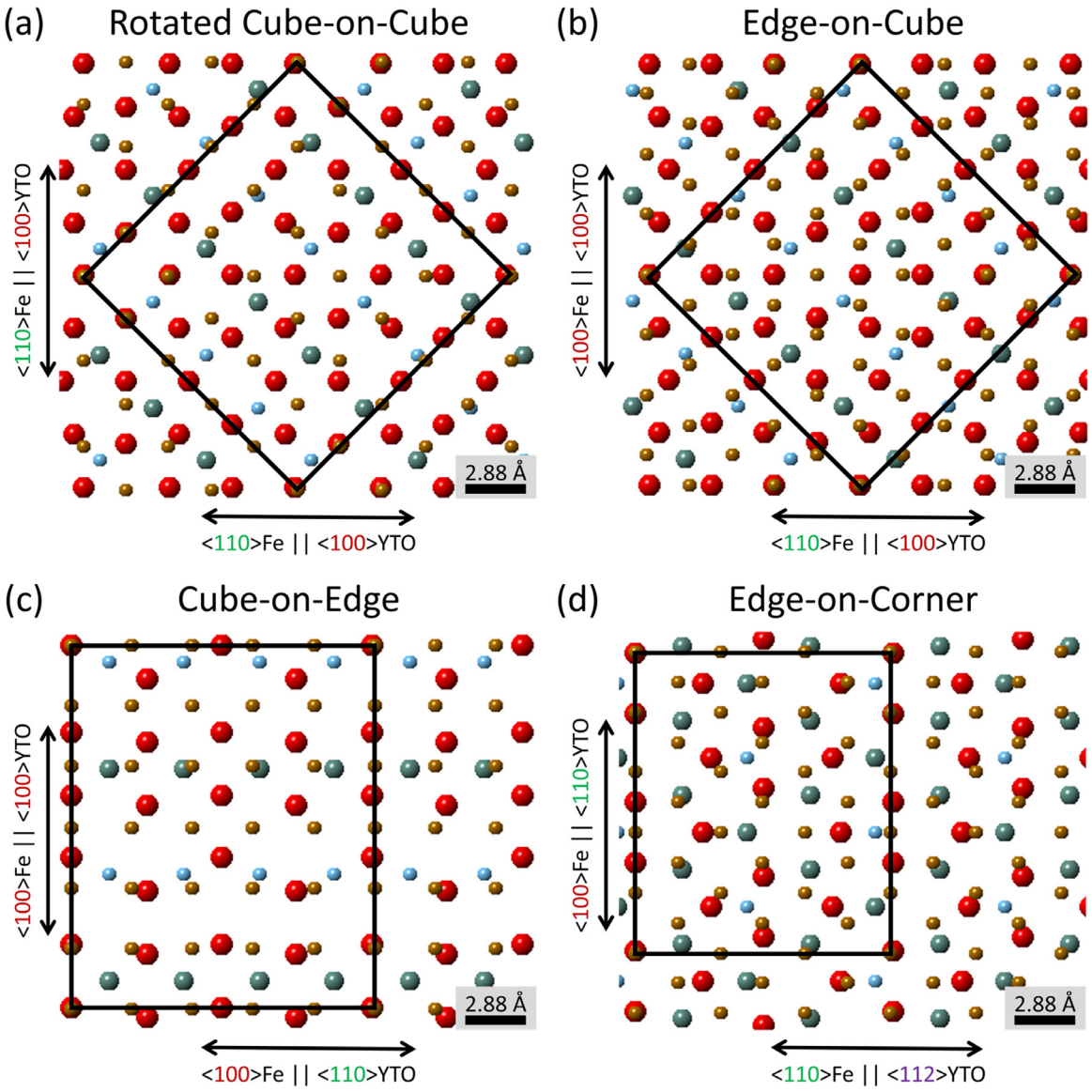

Fig. 8. CrystalMaker renderings of the four orientation relationships observed in this study. Fe atoms are shown in brown, O in red, Y in green, and Ti in light blue. The black rectangles indicate near coincidence site lattices (NCSLs). (For interpretation of the references to colour in this figure legend, the reader is referred to the web version of this article.)

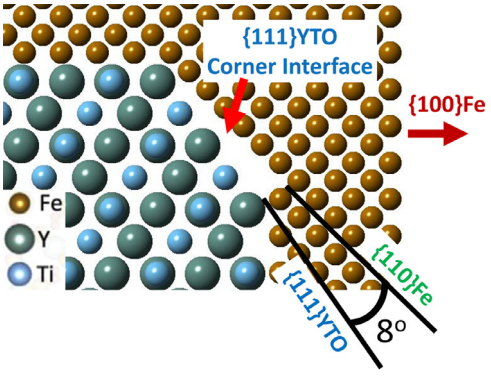

Fig. 9. Un-strained geometric CrystalMaker rendering of the top-right corner of an embedded NO showing the ~8° mismatch between {111}YTO and {110}Fe planes.

tank" for filling bubbles, which further rationalizes the observation that larger NOs are associated with larger bubbles. While the bubbles initially grow on the {111} facets, they eventually envelop the neighboring NO facets (as shown in Fig. 7). For the implantation conditions in this study (1 MeV He^+, 700 °C, 1.2×10^{12} He/cm^2/s, 4.5×10^{16} He/cm^2) the bubbles grow to ~75% of the NO size.

5. Summary and conclusions

To further the understanding of helium behavior in NFAs, a 14YWT alloy was annealed to coarsen the NOs, followed by He implantation to produce bubbles. HRSTEM characterization shows two dominant Fe-$Y_2Ti_2O_7$ orientation relationships (cube-on-edge and cube-on-cube). The smaller NOs are associated with smaller bubbles, while some of the largest NOs (> 6 nm) often have two bubbles. Most bubbles nucleate at {111} NO facets. An updated sequence of events for He trapping and bubble formation is presented. These observations establish a detailed understanding of NO-associated bubble formation that enables efficient He management in NFAs, and also provide a fundamental foundation for first principles modeling efforts. Future studies include additional HRSTEM observations and TEM tomography to confirm the 3D

NO shapes, and electron energy loss spectroscopy (EELS) measurements to obtain the density of helium in bubbles.

Acknowledgment

The authors thank N. Cunningham (UCSB) for annealing the 14YWT alloy, and Y. Jiang (CSU) for fruitful discussions regarding Fe-YTO interface structures and energies. This work was primarily supported by the US DOE, Office of Fusion Energy Sciences, under grant DE-FG03-94ER54275. TEM and EBSD characterization was carried out at the UCSB CNSI Microstructure and Microanalysis Facility, an NSF MRSEC, supported by NSF DMR 1121053. Work at the Lawrence Berkeley National Laboratory Molecular Foundry was supported by the US DOE, Office of Basic Energy Sciences, under contract No. DE-AC02-05CH11231.

References

[1] G.R. Odette, On the status and prospects for nanostructured ferritic alloys for nuclear fission and fusion application with emphasis on the underlying science, Scr. Mater. 143 (2018) 142–148, doi:10.1016/J.SCRIPTAMAT.2017.06.021.
[2] G.R. Odette, Recent progress in developing and qualifying nanostructured ferritic alloys for advanced fission and fusion applications, JOM 66 (2014) 2427, doi:10.1007/s11837-014-1207-5.
[3] S.J. Zinkle, J.L. Boutard, D.T. Hoelzer, A. Kimura, R. Lindau, G.R. Odette, M. Rieth, L. Tan, H. Tanigawa, Development of next generation tempered and ODS reduced activation ferritic/martensitic steels for fusion energy applications, Nucl. Fusion 57 (2017) 1–17.
[4] H. Tanigawa, E. Gaganidze, T. Hirose, M. Ando, S.J. Zinkle, R. Lindau, E. Diegele, Development of benchmark reduced activation ferritic/martensitic steels for fusion energy applications, Nucl. Fusion 57 (2017) 092004, doi:10.1088/1741-4326/57/9/092004.
[5] S.J. Zinkle, J.T. Busby, Structural materials for fission & fusion energy, Mater. Today 12 (2009) 12–19, doi:10.1016/S1369-7021(09)70294-9.
[6] E.E. Bloom, S.J. Zinkle, F.W. Wiffen, Materials to deliver the promise of fusion power – progress and challenges, J. Nucl. Mater. 329 (2004) 12–19, doi:10.1016/j.jnucmat.2004.04.141.
[7] S. Pal, M.E. Alam, S.A. Maloy, D.T. Hoelzer, G.R. Odette, Texture evolution and microcracking mechanisms in as-extruded and cross-rolled conditions of a 14YWT nanostructured ferritic alloy, Acta Mater. 152 (2018) 338–357, doi:10.1016/j.actamat.2018.03.045.
[8] M.E. Alam, S. Pal, S.A. Maloy, G.R. Odette, On delamination toughening of a 14YWT nanostructured ferritic alloy, Acta Mater. 136 (2017) 61–73, doi:10.1016/J.ACTAMAT.2017.06.041.
[9] M.E. Alam, S. Pal, K. Fields, S.A. Maloy, D.T. Hoelzer, G.R. Odette, Tensile deformation and fracture properties of a 14YWT nanostructured ferritic alloy, Mater. Sci. Eng. A. 675 (2016) 437–448, doi:10.1016/j.msea.2016.08.051.
[10] S. Pal, M.E. Alam, G.R. Odette, S.A. Maloy, D.T. Hoelzer, J. Lewandowski, Microstructure, texture and mechanical properties of the 14YWT nanostructured ferritic alloy NFA-1, in: I. Charit, et al. (Eds.), Mechanical and Creep Behavior of Advanced Materials Ch 4, Springer, 2017, pp. 43–54, doi:10.1007/978-3-319-51097-2_4.
[11] N. Cunningham, Y. Wu, D. Klingensmith, G.R. Odette, On the remarkable thermal stability of nanostructured ferritic alloys, Mater. Sci. Eng. A 613 (2014) 296–305, doi:10.1016/j.msea.2014.06.097.
[12] Y. Wu, E.M. Haney, N.J. Cunningham, G.R. Odette, Transmission electron microscopy characterization of the nanofeatures in nanostructured ferritic alloy MA957, Acta Mater. 60 (2012) 3456–3468, doi:10.1016/j.actamat.2012.03.012.
[13] G.R. Odette, D.T. Hoelzer, Irradiation-tolerant nanostructured ferritic alloys: transforming helium from a liability to an asset, JOM 62 (2010) 84–92, doi:10.1007/s11837-010-0144-1.
[14] Y. Dai, G.R. Odette, T. Yamamoto, The Effects of Helium in Irradiated Structural Alloys, 1st ed., Elsevier Inc., 2012, doi:10.1016/B978-0-08-056033-5.00006-9.
[15] S. Chen, Y. Wang, N. Hashimoto, S. Ohnuki, Helium irradiation hardening in Fe, F82H-IEA and F82H-ODS steel, J. Plasma Fusion Res. 11 (2015) 79–82.
[16] P.D. Edmondson, C.M. Parish, Y. Zhang, A. Hallén, M.K. Miller, Helium bubble distributions in a nanostructured ferritic alloy, J. Nucl. Mater. 434 (2013) 210–216, doi:10.1016/j.jnucmat.2012.11.049.
[17] Q. Li, C.M. Parish, K.A. Powers, M.K. Miller, Helium solubility and bubble formation in a nanostructured ferritic alloy, J. Nucl. Mater. 445 (2014) 165–174, doi:10.1016/j.jnucmat.2013.10.048.
[18] T. Stan, The Role of Oxides in Nanostructured Ferritic Alloys and Bilayers: Interfaces, Helium Partitioning and Bubble Formation, University of California Santa Barbara, 2017.
[19] M.J. Alinger, G.R. Odette, D.T. Hoelzer, On the role of alloy composition and processing parameters in nanocluster formation and dispersion strengthening in nanostructured ferritic alloys, Acta Mater. 57 (2009) 392–406, doi:10.1016/j.actamat.2008.09.025.
[20] N.J. Cunningham, Y. Wu, A. Etienne, E.M. Haney, G.R. Odette, E. Stergar, D.T. Hoelzer, Y.D. Kim, B.D. Wirth, S.A. Maloy, Effect of bulk oxygen on 14YWT nanostructured ferritic alloys, J. Nucl. Mater. 444 (2014) 35–38, doi:10.1016/j.jnucmat.2013.09.013.
[21] N.J. Cunningham, Study of the Structure, Composition, and Stability of Y-Ti-O Nm-Scale Features in Nano-Structured Ferritic Alloys, University of California Santa Barbara, 2012.
[22] Y. Wu, J. Ciston, S. Kräemer, N. Bailey, G.R. Odette, P. Hosemann, The crystal structure, orientation relationships and interfaces of the nanoscale oxides in nanostructured ferritic alloys, Acta Mater. 111 (2016) 108–115, doi:10.1016/j.actamat.2016.03.031.
[23] J. Ribis, Y. De Carlan, Interfacial strained structure and orientation relationships of the nanosized oxide particles deduced from elasticity-driven morphology in oxide dispersion strengthened materials, Acta Mater. 60 (2012) 238–252, doi:10.1016/j.actamat.2011.09.042.
[24] J. Ribis, M.A. Thual, T. Guilbert, Y. de Carlan, A. Legris, Relaxation path of metastable nanoclusters in oxide dispersion strengthened materials, J. Nucl. Mater. 484 (2017) 183–192, doi:10.1016/j.jnucmat.2016.12.007.
[25] K. Dawson, G.J. Tatlock, Characterisation of nanosized oxides in ODM401 oxide dispersion strengthened steel, J. Nucl. Mater. 444 (2014) 252–260.
[26] J. Ribis, S. Lozano-Perez, Nano-cluster stability following neutron irradiation in MA957 oxide dispersion strengthened material, J. Nucl. Mater. 444 (2014) 314–322.
[27] M.K. Miller, E.A. Kenik, K.F. Russell, L. Heatherly, D.T. Hoelzer, P.J. Maziasz, Atom probe tomography of nanoscale particles in ODS ferritic alloys, Mater. Sci. Eng. A 353 (2003) 140–145, doi:10.1016/S0921-5093(02)00680-9.
[28] E.A. Marquis, Core/shell structures of oxygen-rich nanofeatures in oxide-dispersion strengthened Fe-Cr alloys, Appl. Phys. Lett. 93 (2008) 10–13, doi:10.1063/1.3000965.
[29] A. Certain, S. Kuchibhatla, V. Shutthanandan, D.T. Hoelzer, T.R. Allen, Radiation stability of nanoclusters in nano-structured oxide dispersion strengthened (ODS) steels, J. Nucl. Mater. 434 (2013) 311–321, doi:10.1016/j.jnucmat.2012.11.021.
[30] C. Hatzoglou, B. Radiguet, P. Pareige, Experimental artefacts occurring during atom probe tomography analysis of oxide nanoparticles in metallic matrix: quantification and correction, J. Nucl. Mater. 492 (2017) 279–291, doi:10.1016/j.jnucmat.2017.05.008.
[31] M. Ohnuma, J. Suzuki, S. Ohtsuka, S.-W. Kim, T. Kaito, M. Inoue, H. Kitazawa, A new method for the quantitative analysis of the scale and composition of nanosized oxide in 9Cr-ODS steel, Acta Mater. 57 (2009) 5571–5581, doi:10.1016/j.actamat.2009.07.054.
[32] T. Stan, D.J. Sprouster, A. Ofan, G.R. Odette, L.E. Ecker, I. Charit, X-ray absorption spectroscopy characterization of embedded and extracted nano-oxides, J. Alloys Compd. 699 (2017) 1030–1035, doi:10.1016/j.jallcom.2016.12.350.
[33] S. Liu, G.R. Odette, C.U. Segre, Evidence for core–shell nanoclusters in oxygen dispersion strengthened steels measured using X-ray absorption spectroscopy, J. Nucl. Mater. 445 (2014) 50–56, doi:10.1016/j.jnucmat.2013.10.042.
[34] A.J. London, B.K. Panigrahi, C.C. Tang, C. Murray, C.R.M. Grovenor, Glancing angle XRD analysis of particle stability under self-ion irradiation in oxide dispersion strengthened alloys, Scr. Mater. 110 (2016) 24–27, doi:10.1016/j.scriptamat.2015.07.037.
[35] M. Dumont, L. Commin, I. Morfin, F. DeGeuser, F. Legendre, P. Maugis, Chemical composition of nano-phases studied by anomalous small-angle X-ray scattering: application to oxide nano-particles in ODS steels, Mater. Charact. 87 (2014) 138–142, doi:10.1016/j.matchar.2013.11.008.
[36] L. Yang, Y. Jiang, G. Robert Odette, T. Yamamoto, Z. Liu, Y. Liu, Trapping helium in $Y_2Ti_2O_7$ compared to in matrix iron: a first principles study, J. Appl. Phys. 115 (2014) 143508, doi:10.1063/1.4871282.
[37] L. Yang, Y. Jiang, Y. Wu, G.R. Odette, Z. Zhou, Z. Lu, The ferrite/oxide interface and helium management in nano-structured ferritic alloys from the first principles, Acta Mater. 103 (2016) 474–482, doi:10.1016/j.actamat.2015.10.031.
[38] L. Barnard, N. Cunningham, G.R. Odette, I. Szlufarska, D. Morgan, Thermodynamic and kinetic modeling of oxide precipitation in nanostructured ferritic alloys, Acta Mater. 91 (2015) 340–354, doi:10.1016/j.actamat.2015.03.014.
[39] T. Liu, L. Wang, C. Wang, H. Shen, H. Zhang, Feasibility of using $Y_2Ti_2O_7$ nanoparticles to fabricate high strength oxide dispersion strengthened Fe–Cr–Al steels, Mater. Des. 88 (2015) 862–870, doi:10.1016/J.MATDES.2015.08.118.
[40] Y. Miao, K. Mo, B. Cui, W. Chen, M.K. Miller, K.A. Powers, V. Mccreary, D. Gross, J. Almer, I.M. Robertson, J.F. Stubbins, The interfacial orientation relationship of oxide nanoparticles in a hafnium-containing oxide dispersion-strengthened austenitic stainless steel, Mater. Charact. 101 (2015) 136–143, doi:10.1016/j.matchar.2015.01.015.
[41] V. Badjeck, M.G. Walls, L. Chaffron, J. Malaplate, K. March, New insights into the chemical structure of $Y_2Ti_2O_{7-\delta}$ nanoparticles in oxide dispersion-strengthened steels designed for sodium fast reactors by electron energy-loss spectroscopy, J. Nucl. Mater. 456 (2015) 292–301.
[42] G.R. Odette, M.J. Alinger, B.D. Wirth, Recent developments in irradiation-resistant steels, Annu. Rev. Mater. Res. 38 (2008) 471–503, doi:10.1146/annurev.matsci.38.060407.130315.
[43] L. Yang, Y. Jiang, G.R. Odette, W. Zhou, Z. Liu, Y. Liu, Nonstoichiometry and relative stabilities of $Y_2Ti_2O_7$ polar surfaces: a density functional theory prediction, Acta Mater. 61 (2013) 7260–7270.
[44] Oxford Instruments, CHANNEL 5 User Manual, 2007.
[45] T. Stan, Y. Wu, P.B. Wells, H.D. Zhou, G.R. Odette, Epitaxial fe thin films on {100} $Y_2Ti_2O_7$: model interfaces for nano-oxide dispersion strengthened steels, Metall. Mater. Trans. A. (2017), doi:10.1007/s11661-017-4283-7.
[46] T. Stan, Y. Wu, G.R. Odette, K.E. Sickafus, H.A. Dabkowska, B.D. Gaulin, Fabrication and characterization of naturally selected epitaxial FE-{111} $Y_2Ti_2O_7$

mesoscopic interfaces: some potential implications to nano-oxide dispersion-strengthened steels, Metall. Mater. Trans. A Phys. Metall. Mater. Sci. 44 (2013) 4505–4512, doi:10.1007/s11661-013-1827-3.
[47] S. Choudhury, D. Morgan, B.P. Uberuaga, Massive interfacial reconstruction at misfit dislocations in metal/oxide interfaces, Sci. Rep. 48 (2017) 5658–5666, doi:10.1038/srep06533.
[48] D.A. Porter, K.E. Easterling, M.Y. Sherif, Phase Transformations in Metals and Alloys, 3rd ed., CRC Press, Boca Raton, 2009.
[49] K. Ralls, T. Courtney, J. Wulff, Introduction to Materials Science and Engineerinig, Wiley, 1976.
[50] K.-W. Benz, W. Neumann, Introduction to Crystal Growth and Characterization, Wiley-VCH, 2014.
[51] T. Furuhara, T. Kimori, T. Maki, Crystallography and interphase boundary of (MnS + VC) complex precipitate in austenite, Metall. Mater. Trans. A 37A (2006) 951.
[52] J.M. Rigsbee, H.I. Aaronson, A computer modeling study of partially coherent F.C.C.:B.C.C. boundaries, Acta Metall. 27 (1979) 351–363.
[53] Q. Liang, W.T. Reynolds, Determining interphase boundary orientations from near-coincidence sites, Metall. Mater. Trans. A Phys. Metall. Mater. Sci. 29 (1998) 2059–2072, doi:10.1007/s11661-998-0032-2.